# Monitoring fluid migration using in-situ nuclear magnetic resonance core flooding system integrated with fiber optic sensors: A proof of concept

*Bruno* da Silva Falcão[1,2,*], *Lionel* Esteban[2], *Ausama* Giwelli[2], *Yevhen* Kovalyshen[2], *Stephen* Banks[2], *Ahmed* Al-Yaseri[1,3], *Alireza* Keshavarz[1], and *Stefan* Iglauer[1]

[1]School of Engineering, Edith Cowan University, Joondalup, WA 6027, Australia
[2]CSIRO Energy Business Unit, Kensington, WA 6151, Australia
[3]Currently at School of Engineering, Curtin University, Kensington, WA 6151, Australia

**Abstract.** In-situ nuclear magnetic resonance (NMR) core flooding system has enabled researchers to monitor several rock properties such as porosity, pore size distribution, and fluid saturation along the tested samples with high resolutions and under reservoir conditions. However, spatially resolved rock strength/mechanical property alteration coupled to fluid migration/substitution remains poorly characterized. To this end, Fiber Bragg Grating (FBG) multiplex sensors were integrated with NMR core flooding system to monitor rock strength changes, or generally speaking, to observe hydro-mechanical-chemical coupling mechanisms during core flooding tests. In this study, we present a novel approach on how to conduct core flooding experiments, while simultaneously monitoring NMR and FBG strain response of the tested limestone plug. The NMR cell was modified to integrate FBG technology without impeding the NMR signal and core flooding high pressure/temperature capacity. A high spatial resolution optical fiber was attached onto the sample radial surface. The results show the successful association of NMR and FBG sensors to track any change at each stage of brine injection. The FBG is capable of measuring the rock strain variations induced by rock-fluid interactions during brine injection, allowing it to capture the fluid front location along with the sample and at a faster rate than the NMR.

## 1 Introduction

Nuclear magnetic resonance (NMR) core flooding system became an important tool for reservoir rock characterizations [1-3]. It enables the evaluation of several rock properties such as porosity, pore size distribution, and fluid saturation to name a few with high resolution and under reservoir conditions [4-6].

Likewise, the evaluation of rock mechanical properties also plays an important role in reservoir characterization, especially for risk assessment and economic production sustainability. Measuring rock strength changes is essential under reservoir conditions, even more when the rock experiences potential mineralogy alteration during fluids displacements, which can lead to rock deformations, faults reactivation, reservoir leakage pathways [7], and the like. Conventionally, rock strain deformations are measured by linear variable differential transformers (LVDTs) and electrical resistance strain gauges (ESG) [8-10]. However, those conventional sensors are incompatible with the NMR core flooding system as the small confining space and the magnet in-place of the NMR probe prohibit the insertion of such metallic sensors.

Optical fibers were introduced in the 1960s with the sole purpose of transmitting light, which later had a positive impact on telecommunication systems. However, due to the change in the transmitted light properties by the nearby environment, optical fibers were considered a good option for sensing applications [11]. Fiber optic sensors (FOS) have been applied in a vast variety of industries from aerospace [12], medicine [13], civil engineering [14] to petroleum [15]. FOS can be classified into two main categories: distributed and discrete. Distributed FOS is based on Raman, Rayleigh, or Brillouin scattering mechanisms and measure changes all along the fiber's length. Discrete FOS, however, such as fiber Bragg grating and Fabry-Perot, provide information at specific locations [14, 16]. Fiber Bragg Grating (FBG) sensors can be multiplexed enabling them to measure changes at different locations using a single fiber being considered as a quasi-distributed sensor [14].

FBG sensor is a very promising deformation measurement tool acting as an alternative to the conventional sensors [8-10, 17] with less sensors-sample setup time, more efficient, and cost-effective. It is capable of measuring strain, temperature, pressure, among other parameters. FBG sensors also offer the advantages of being small size, flexible, low weight, high sensitivity, not affected by electromagnetic interference, resistant to corrosion and water, resilient to high-pressures and high-temperatures, and multiplexing capability [8, 10].

In recent years, the application of FBG sensors to monitor rock strain changes in real-time at laboratory scale has expanded and it seems to be a good alternative to LVDTs or ESG but it is still in the exploration stage. Sun et al. [8] proposed the use of multichannel FBG sensor arrays to monitor rock strain. The authors measured both radial and axial strains on the lateral area of a sandstone sample undergoing a uniaxial loading. Sun et al. [9] also employed multichannel FBG sensors to detect strain responses caused by water and $CO_2$ gas injection during core flooding experiments through a low permeability sandstone. Kovalyshen et al. [10] reported the applicability of FBG sensors to measure strain variations of a limestone sample

* Corresponding author: bruno.falcao@msn.com

under confining pressure. Zhang et al. [17] tracked the $CO_2$/brine displacement front in a rock sample composed of both reservoir and caprock formations. The fluid displacement was monitored by measuring the strain using the distributed fiber optic strain sensing (DFOSS) technique. X-ray computed tomography imaging was used to estimate the fluid saturation.

In this paper, we present a novel approach on how to conduct core flooding experiments associating NMR core flooding system with FBG sensing technology. To our knowledge, this is the first NMR core flooding experiment that is capable of measuring rock strain deformations at reservoir conditions. An optical fiber with 8 FBG sensors was radially placed around the rock sample surface to monitor the rock strain deformations induced by brine injection while under reservoir pressure condition. The NMR core analyzer was used to monitor the fluid displacement and saturation along the sample throughout the experiment.

## 2 Material and methods

### 2.1 Principle of FBG sensing

A Fiber Bragg Grating (FBG) sensor is an optical deflector or filter of specific wavelength responses. Its functioning relies on the optical fiber core's refractive index being periodically altered by UV light. When a light source is emitted into the FBG sensor, it reflects part of the energy in a limited wavelength band around its peak wavelength and transmits all other wavelengths. The reflected wavelength is known as Bragg wavelength $\lambda_B$ and it is defined by Equation (1) [8-10, 18, 19].

$$\lambda_B = 2n_{eff}\Lambda \tag{1}$$

where $n_{eff}$ is the FBG core's effective refraction index and $\Lambda$ is the grating spacing. Modifications on $n_{eff}$ or $\Lambda$ values, or even a combination of both, will represent any changes that occur in the physical properties such as strain and temperature [8-10, 18, 19].

The shift in the Bragg wavelength caused by changes in the strain and temperature is given by Equation (2).

$$\Delta\lambda_B = 2\left(\Lambda\frac{\partial n_{eff}}{\partial l} + n_{eff}\frac{\partial \Lambda}{\partial l}\right)\Delta l + 2\left(\Lambda\frac{\partial n_{eff}}{\partial T} + n_{eff}\frac{\partial \Lambda}{\partial T}\right)\Delta T \tag{2}$$

The first term in Equation (2) represents the change in the Bragg wavelength due to the strain effect, while the second term describes the effect of temperature [18, 19].

For the FBG used in this study, the wavelength sensitivity coefficient related to strain and temperature at room conditions, according to the manufacturer, are 0.776 pm/με, 8.53 pm/ºC, and 0.0023 pm/ºC. The optical fiber was manufactured by FBGS (FBGS Technologies GmbH), with 125 μm cladding diameter and Ormocer coating. Each single optical fiber has 8 FBG sensors of low bend loss and every sensor is 8 mm long. The eight gratings cover an extent of 315 mm ranging from 1530 to 1565 nm wavelength, with a difference of 5 nm between the gratings to avoid overlap.

### 2.2 Nuclear magnet resonance (NMR)

When an external magnetic field is applied, protons $^1H$ (abundant in reservoir fluids) behave like spinning magnets due to their magnetic moment and angular momentum [4, 6]. Rotational proton procession produces signals that decay with time also known as proton relaxation that can be measured by a Nuclear Magnetic Resonance spectrometer (NMR) [4, 6].

The NMR signal decay **M**(t) is described by Equations (3)–(5) from two mechanisms: NMR signal can be measured along the applied magnetic field corresponding to proton polarization or longitudinal relaxation $T_1$; while the proton decay post-polarization and then tipped transversally to the magnetic field corresponds to the transversal relaxation $T_2$ [4, 20, 21].

$$M_x(t) = \left[M_x(0)\cos(\omega t) - M_y(0)\cos(\omega t)\right]e^{(-t/T_2)} \tag{3}$$

$$M_y(t) = \left[M_x(0)\cos(\omega t) - M_y(0)\cos(\omega t)\right]e^{(-t/T_2)} \tag{4}$$

$$M_z(t) = M_{eq} + \left[M_z(0) - M_{eq}\right]e^{(-t/T_1)} \tag{5}$$

Generally speaking, on very porous rock materials, $T_1$ is sensitive to the environment and fluids interactions while $T_2$ is more sensitive to surface relaxation and diffusion mechanisms. With negligible fluids interactions, both $T_1$ and $T_2$ provide pore size distribution information, though $T_1$ measurement is more time consuming than $T_2$ [6].

A 2.37 MHz Geospec2 NMR core analyzer and a P5 overburden NMR probe from Oxford Instruments were used to obtain the brine saturation profile along the sample.

### 2.3 Sample preparation and characterization

A Savonnières limestone core (Fig. 1), a heterogeneous rock composed of 99% of calcite [22-24], was used in this study and cut along the bedding plane. The yellow dashed lines in Fig. 1 highlight a centimeter-thick bedding composed of high-density/low porosity structure that pervades the middle of the sample. This tight bedding is better illustrated in Fig. 2, which shows a 3D volume rendering from X-ray CT images viewed in two angles color-labeled by density intensity from single threshold method on the X-ray CT attenuation histogram where magenta color corresponds to a highly porous area while yellow color marks much denser and tighter material. The images illustrate that the tight bedding is actually composed of alternating thin-sub layers of high- and low-density materials with some thin dense layers propagating toward one side of the sample. The plug can then be divided into three structural areas along the sample from left to right in Fig. 2: (1) 1.5 cm thick highly porous layer, (2) 1.5 cm thick tight layer, and (3) < 1 cm thin highly porous layer. Table 1 shows the location of the sensors on the sample with respect to the described structural layers: (i) sensors facing the section with the highest void fraction with sensors

1, 4, 5, and 7; (ii) sensors facing the section with the lowest void fraction with sensors 3 and 6; (iii) sensors located perpendicular to the beddings with sensors 2 and 8. The dimension of the tested plug is shown in Fig. 1. The sample was initially dried at 60 ºC under air vacuum for 24 hours before attaching FBG wire and then place the assembly in the NMR core flooding system. Further details about the rock properties can be found in the open literature [22, 23, 25].

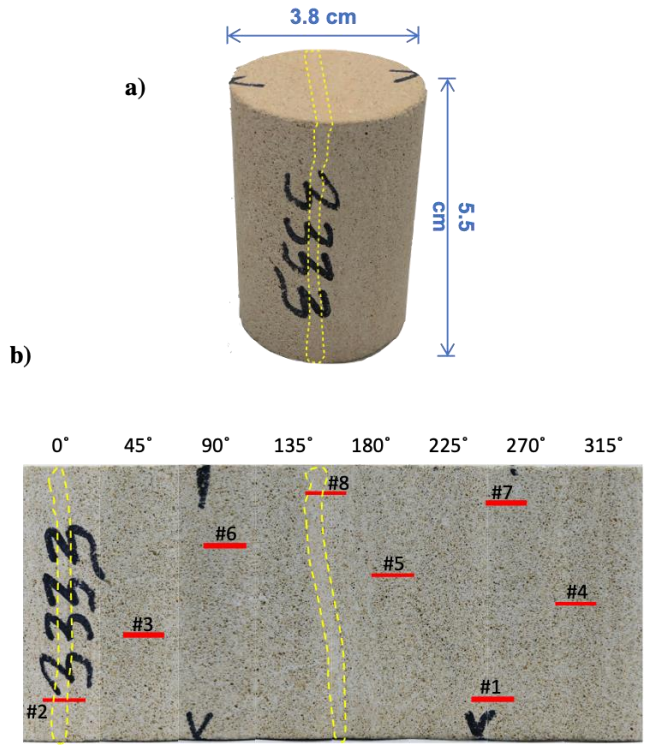


Fig. 1. (a) Savonnières limestone sample used in this experiment. (b) Position of FBG sensors on the sample after unwrapping the plug surface. The dashed yellow area indicates the position of a bedding of higher density/lower porosity.

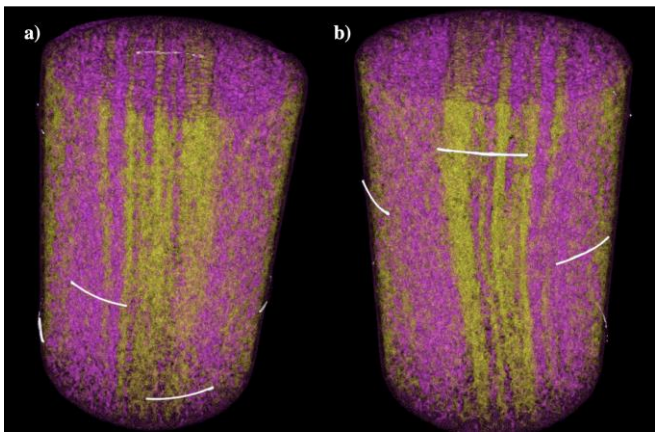


Fig. 2. 3D volume rendering from X-ray CT images of Savonnières limestone sample. The color magenta represents the pores of the rock sample, the yellow represents the existing beddings of higher density in the middle of the sample, and the white (enhanced) indicates the sensors' location. (a) Front view of the sample showing the sensors 3, 2, 4, and 1 at the bottom (from right to left). (b) back view of the sample showing the sensors 5, 8, and 6 (from right to left).

Table 1. Position of the FBG sensors related to the void fractions and beddings.

| Category | Sensor | Description |
|---|---|---|
| (i) | 1, 4, 5, 7 | Facing the section with the highest void fraction. |
| (ii) | 3, 6 | Facing the section with the lowest void fraction. |
| (iii) | 2, 8 | Perpendicular to the beddings. |

The optical fiber was spirally attached onto the sample surface using Loctite Super Glue All Plastics and cured for 24 h. This glue adequately couples the optical fiber with the rock surface, without modifying the rock stiffness properties [10]. The position of the sensors is shown in Fig. 1 and Table 2. For the core flooding test, the FBG wire was inserted through the pore fluid line using a modified end-platen, specifically designed for this experiment. A feedthrough component was used to prevent any leakage while the system was pressurized. After the curing process, the whole assembly was covered by a Teflon heat shrink jacket and a Viton sleeve and then placed inside the NMR P5 probe.

The optical fiber was connected to a FAZT I4 optical interrogator (FAZ Technology) through an LC/APC connector at the lead-in. The optical interrogator is capable of detecting wavelengths ranging from 1529 to 1568.2 nm, which limits the total number of sensors to eight due to the 5 nm grating difference.

Table 2. Position of FBG sensors: the distance was measured from the bottom of the sample to the center of the FBG sensor.

| Sensor | Distance (mm) |
|---|---|
| 1 | 7.8 |
| 2 | 8.2 |
| 3 | 20.9 |
| 4 | 26.9 |
| 5 | 32.6 |
| 6 | 38.1 |
| 7 | 46.7 |
| 8 | 48.4 |

## 2.4 Testing procedure

The P5 probe assembly was inserted into the NMR spectrometer and a constant hydrostatic confining pressure of 1000 psi was applied at a rate of 50 psi/min using Fluorinert as confining fluid. After stabilization of the confining

pressure, dopped brine with 5 g/L $NiCl_2$ was continuously injected at 0.1 cc/min from the bottom of the sample.

During the imbibition/saturation stage, the outlet of the system was open to the atmosphere such as the FBG sensors can accurately and slowly track the brine front by recording the changes in the strain values. A 200 psi backpressure was then applied, to monitor the effect of pore pressure change on the FBG sensors during brine injection at 0.1 cc/min.

Fig. 3 shows the confining and pore pressure data during the entire experiment. Section I refers to the brine injection while the outlet was open to the atmosphere. Section II represents the period during which the injection was stopped to connect the backpressure regulator. Section III shows the pore pressure behavior after the backpressure was activated and set at 200 psi.

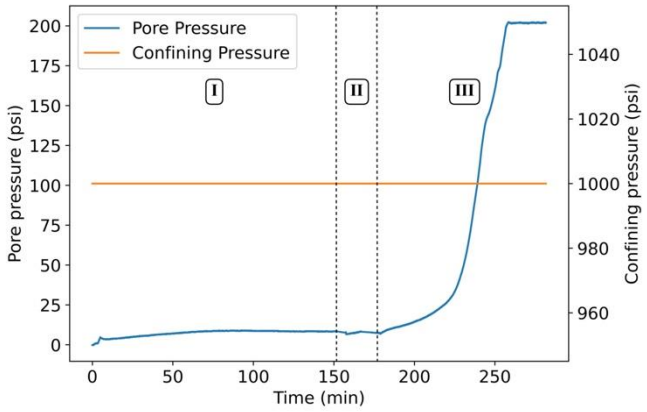


Fig. 3. Pore pressure and confining pressure monitoring with time during imbibition exercise on Savonnières sample under 1000 psi confining pressure: I – brine injection at 0.1 cc/min while outlet was open to the atmosphere; II –injection stopped to connect the backpressure; III – backpressure activated and set to 200 psi.

Three Teledyne ISCO syringe pumps were used to control the confining pressure, pore pressure, and backpressure. All pressure values were recorded using in-house LabView code. The entire experiment was performed at a constant temperature of 22 °C in order to avoid any temperature interference on the strain measurement. To obtain that the NMR system is connected to external chiller throughout the experiment.

### 2.5 Data acquisition and processing

During the experiment, all the measured NMR data were collected and computed automatically via Green Imaging Technologies software [26, 27]. Water content profile along the sample used the following settings:

Recycle delay: 3750 ms
Tau: 500 µs
Gradient duration: 300 µs
Filter width: 125 kHz
Resolution: 64

A data acquisition system, using LabView, was designed to continually log the data from the syringe pumps every second. The optical interrogator systems enable the streaming of the data over an ethernet connection. The FBG data acquisition and graphical display software ran on a PC via an ethernet connection (0.1 Gbit/s) at a sampling rate of 1000 Hz. An in-house algorithm was developed to process the raw data and generate all the relevant figures.

## 3 Results and discussion

### 3.1 Confining pressure and strain

In the first stage of the experiment, the objective was to analyze the relationship between confining pressure and rock strain changes in dry state. Initially, the confining pressure was increased from 20 psi to 1000 psi at a rate of 50 psi/min as shown in Fig. 4. After the confining pressure reached 1000 psi, it was temporarily decreased to 885 psi (after ~ 22 min) and kept constant for a few minutes. FBG strain changes caused by the increase in the confining pressure are shown in Fig. 5, which demonstrates the good agreement between the changes in the confining pressure and the rock strain responses. Fig. 5 highlights some different sensor behaviors while the confining pressure increases or decreases. Though most of the sensor responses can be explained from the structural heterogeneities observed in Fig. 1 and Fig. 2, sensors 2 and 3 showed similar responses to the changes in the confining pressure while being within distinct structural areas (Fig. 1). This was also observed for sensors 5 and 8. As depicted in Fig. 6, the strain values of all sensors decreased with the increase in the confining pressure. As a result, the temporary changes in the confining pressure demonstrated the fast and accurate response of the FBG sensors. The final strain values at a constant confining pressure of 1000 psi ranged from -250 to -350 µε.

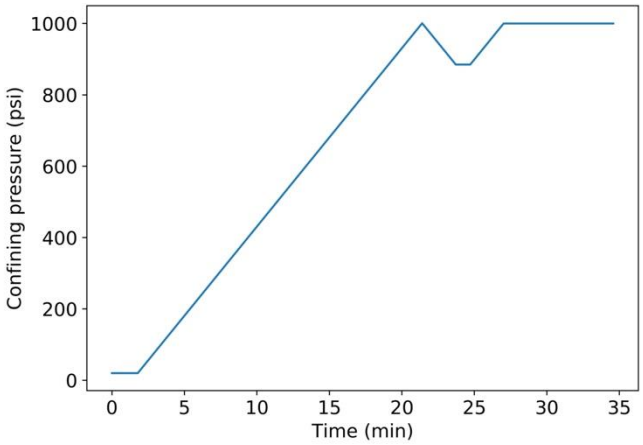


Fig. 4. Confining pressure profile prior to the brine injection.

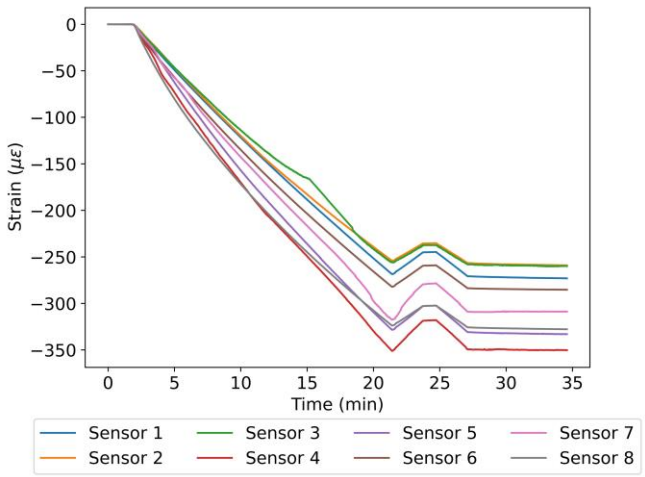


Fig. 5. Corresponding strain changes on the dry rock during the confining pressure build-up, measured by FBG sensors.

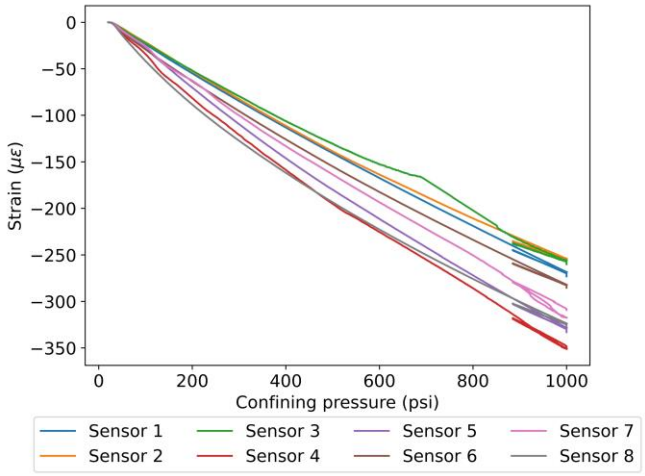


Fig. 6. Measurements of strain at varying confining pressures for each sensor, measured during the build-up of the confining pressure on dry rock.

### 3.2 Brine front monitoring

In order to monitor the fluid migration with FBG sensors, we kept the outlet pore line opens to the atmosphere, section I in Fig. 3. This brine injection continues until breakthrough occurred, once the brine came out of the sample. Pore pressure was as low as 9 psi, at a 0.1 cc/min brine flow rate.

Fig. 7 illustrates that the FBG sensors effectively monitored the brine front during the injection process. It is possible to identify the location of the brine front in the rock sample at a specific time by monitoring the rock strain changes. The strain changes corresponded well to the fluid migration, and all sensors exhibited an increase in the strain when the fluid reached the sensor location. The differential strain kept increasing to values between 2 and 3 με, until the brine breakthrough.

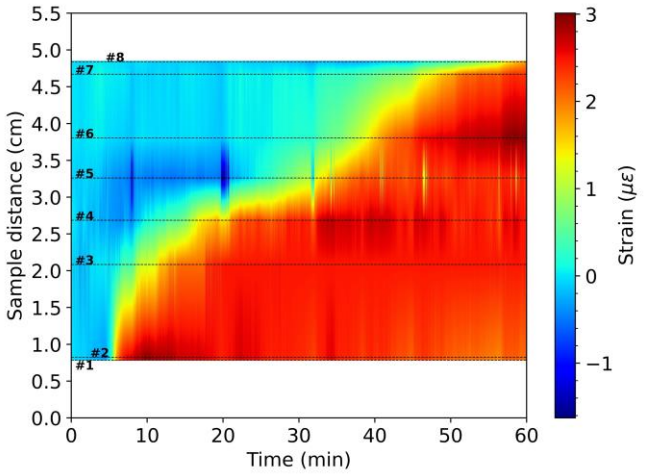


Fig. 7. Mapping of the strain changes throughout the sample until the brine breakthrough. The locations of the sensors are labeled on the figure in dashed lines. Note that the differential strain data were linearly interpolated between the sensors. Information about strain changes before sensor 1 and after sensor 8 is unavailable.

The saturation profiles measured by NMR are shown in Fig. 8. The NMR saturation profile provides information about the migration of the fluid front and the corresponding volume distribution of the fluid within the sample. The results from both FBG and NMR are in good agreement. For instance, it can be estimated that the brine front reached sensor 4 after approximately 10 minutes. However, while the FBG interrogator was recording 1000 points/second, the NMR core analyzer took approximately 2 minutes to acquire each saturation profile measurement. Therefore, the combination of FBG sensors with NMR analysis allows a more accurate time tracking of the fluid front migration during core flooding experiments. It is worth mention that after about 60 mins of injection, the sample did not show uniform saturation distribution. This could be due to air bubble at the top of the sample not fully removed yet or permeability impediment during imbibition.

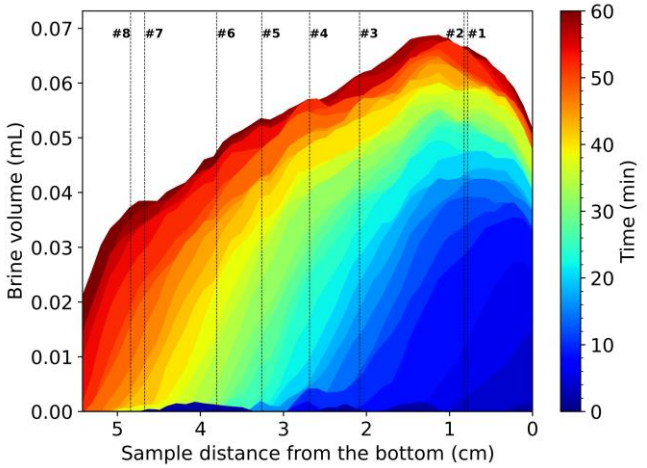


Fig. 8. NMR saturation profiles along the length of the sample.

### 3.3 Pore pressure effect

After the brine breakthrough occurred, a backpressure regulator was applied. A backpressure regulator at 200 psi was used with the purpose to analyze the effect of the pore pressure on the FBG sensors. After the activation of the backpressure, the pore pressure started to increase, while keeping brine injected at 0.1 cc/min, as shown in Fig. 3 (section III).

Fig. 9 shows the FBG strain changes from each sensor during the entire experiment. Comparing sections I and III in Fig. 9, it is observed that the increase in the pore pressure caused higher changes in the strain values. While the strain changes in section I were between 2 and 3 με, the strain changes increased to values between 30 and 50 με at the end of section III. This change can be explained by Fig. 10, which shows that an increase in the pore pressure causes an increase in the strain measurements of all sensors.

According to Fig. 9 and Fig. 10, each sensor shows a different strain behavior while the pore pressure is increased, mainly due to rock heterogeneity and internal pore structure (see Fig. 1 and Fig. 2). For instance, sensors 4 and 5, glued on the permeable region of the rock, see Table 1, showed the highest strain value/deformation among the sensors. On the other hand, sensors 2 and 3, glued on/near the bedding area, see Table 1, shows the least strain value. This is a clear indication that all the FBG sensors were very sensitive to detect the internal pore fluid distribution of the sample. As pore pressure is gradually increased inside the rock, brine navigating its way through more permeable section, the pore pressure distribution is not uniform anymore, and accordingly, the net overburden pressure acting on the sample surface is not uniform. It is worth noting that, we anticipated sensor 8 would behave similarly to sensor 2 (see Table 1), but surprisingly the sensor 8 showed a higher deformation. This could be due to test platen effects that caused more damage around the sensor area.

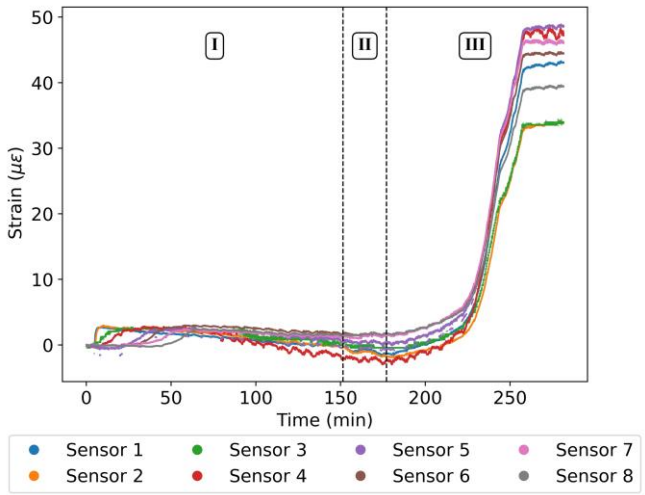


Fig. 9. Strain changes, measured by FBG sensors, during the entire experiment: I – brine injection at 0.1 cc/min while the outlet section was open to the atmosphere; II – injection paused to connect the backpressure; III – backpressure activated and set to 200 psi.

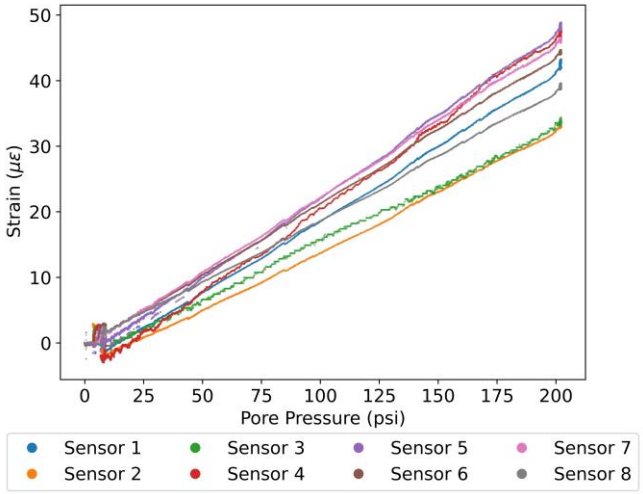


Fig. 10. Differential strain measurements at varying pore pressures for each sensor, measured during the pore pressure build-up.

## 4 Conclusion

In this study, a new method is presented to perform NMR core flooding experiments associated with fiber optic sensing technology. FBG array of 8 sensors were employed to monitor rock strain induced by the brine injection. We demonstrated that the FBG sensors responded quickly and accurately to the changes in the confining pressure, pore pressure and also were able to track the fluid migration through the Savonnières sample. In addition, we showed that the response of the FBG sensors was related to the sample's structure. Sensors facing the high void fraction sector of the sample were more sensitive to both confining and pore pressure changes than the sensors facing the lower void fraction sector (i.e. denser material).

Prior to brine injection, the confining pressure was increased to 1000 psi and kept constant throughout the experiment stages. The FBG measured changes in the rock strain with high accuracy caused by the increase in the confining pressure, showing an inversely proportional behavior. During the first stage of the brine injection, the outlet was kept open to the atmosphere to capture the fluid front migration. The FBG sensors demonstrated the capability of monitoring the fluid front migration, determining its location along the sample, at a faster rate and higher resolution than the NMR system. After the brine breakthrough, a backpressure regulator was activated to analyze the effect of pore pressure build-up on the FBG strain measurements.

In summary, this pilot experiment proves to be useful to monitor rock strain changes during NMR core flooding stages. Future studies are planned to assess the behavior of different rock types, injection fluids, including $CO_2$.

The first author acknowledges Edith Cowan University's financial support. We also acknowledge the financial support provided by CSIRO Energy Business Unit through a Strategic Research Fund.

## References


1. M. Li, D. Xiao, M. Shakerian, A. Afrough, F. Goora, F. Marica, L. Romero-Zerón, and B. Balcom, International Symposium of the Society of Core Analysts, Snowmass, Colorado, 21-26 (2016)
2. T. Hiller, G. Hoder, A. Amann-Hildenbrand, N. Klitzsch, and N. Schleifer, E3S Web of Conferences, 03005 (2020)
3. S. Hua, Y. Li, and Q. Di, E3S Web of Conferences, (2020)
4. G. R. Coates, L. Xiao, and M. G. Prammer, *NMR logging: principles and applications* (Haliburton Energy Services Houston, 1999)
5. J. Mitchell, T. C. Chandrasekera, D. J. Holland, L. F. Gladden, and E. J. Fordham, Phys. Rep., **526**, 165-225 (2013)
6. C. McPhee, J. Reed, and I. Zubizarreta, *Core analysis: a best practice guide* (Elsevier, 2015)
7. J. Rutqvist, and C.-F. Tsang, Environ. Geol., **42**, 296-305 (2002)
8. Y. Sun, Q. Li, D. Yang, C. Fan, and A. Sun, Eng. Geol., **213**, 1-10 (2016)
9. Y. Sun, Q. Li, and C. Fan, Int. J. Greenh. Gas Control., **60**, 186-198 (2017)
10. Y. Kovalyshen, S. Banks, and A. Giwelli, 52nd US Rock Mechanics/Geomechanics Symposium, (2018)
11. X. Qiao, Z. Shao, W. Bao, and Q. Rong, Sensors (Basel), **17**, (2017)
12. P. F. Díaz-Maroto, A. Fernández-López, J. García-Alonso, M. Iglesias, and A. Güemes, Thin-Walled Struct., **132**, 375-384 (2018)
13. J. Heijmans, L. Cheng, and F. Wieringa, 4th European Conference of the International Federation for Medical and Biological Engineering, 2330-2334 (2009)
14. H.-N. Li, D.-S. Li, and G.-B. Song, Eng. Struct, **26**, 1647-1657 (2004)
15. C. S. Baldwin, Fiber Optic Sensors and Applications XII, 94800D (2015)
16. B. Glisic, and Y. Yao, Struct. Health Monit., **11**, 696-711 (2012)
17. Y. Zhang, Z. Xue, H. Park, J. Q. Shi, T. Kiyama, X. Lei, Y. Sun, and Y. Liang, Water Resour. Res., **55**, 856-867 (2019)
18. L. Grattan, and B. Meggitt, *Optical fiber sensor technology: advanced applications-Bragg gratings and distributed sensors* (Springer Science & Business Media, 2013)
19. C. E. Campanella, A. Cuccovillo, C. Campanella, A. Yurt, and V. M. N. Passaro, Sensors (Basel), **18**, (2018)
20. I. B. Trindade, and R. O. Louro: 'Introduction to biomolecular nuclear magnetic resonance and metals': 'Practical Approaches to Biological Inorganic Chemistry' (2020), pp. 155-199
21. P. R. Connolly, J. Sarout, J. Dautriat, E. F. May, and M. L. Johns, Petrophysics-The SPWLA Journal of Formation Evaluation and Reservoir Description, **61**, 151-161 (2020)
22. M. Seyyedi, H. K. B. Mahmud, M. Verrall, A. Giwelli, L. Esteban, M. Ghasemiziarani, and B. Clennell, Sci Rep, **10**, 3624 (2020)
23. A. Raza, R. Gholami, and M. Sarmadivaleh, AAPG Bull., **103**, 83-96 (2020)
24. Y. Zhang, M. Lebedev, M. Sarmadivaleh, A. Barifcani, and S. Iglauer, SPE asia pacific oil & gas conference and exhibition, (2016)
25. M. Lebedev, M. E. J. Wilson, and V. Mikhaltsevitch, Geophys. Prospect., **62**, 1253-1265 (2014)
26. Geo-Spec 2-53 User Manual, Version 1.8, Oxford Instruments
27. GIT Systems and LithoMetrix User Manual, Revision 1.9, Green Imaging Technologies